Supplement to: BrCN in the global troposphere

1 Formation of BrCN from HOBr chemistry

The formation of XCN compounds from reactions of HCN/CN^- in the condensed phase is well known, so deserves consideration in the context of the polar boundary layer. The major sources of HCN to the atmosphere are biomass burning and vehicle exhaust, two sources that favor the northern hemisphere. HCN is a very weak acid (pKa=9.3), is not very soluble in water (Yoo et al., 1986), and its gas phase loss processes are quite slow (several years against reaction with OH). Consequently, HCN is widely distributed throughout the troposphere as is apparent in the ATom data shown in the main text. Vertical profiles of HCN imply a surface sink and the effective lifetime of HCN has been estimated to be about 5 months (Li et al., 2003). The data from ATom-3&4, including the vertical profile and inter-hemisphere distribution, are for the large part in agreement with this.

There are many parameters that go into a model description of polar bromine chemistry, some of them fairly uncertain (for example rate constants at cold temperatures). One way to isolate and examine how BrCN formation from HCN might impact the active-bromine cycle is to compare the rates of liquid phase chemistry that perpetuates the Br cycle, to the chemistry that would remove active Br by making BrCN:

$$Br_2 + HCN \rightarrow BrCN + Br^- + H^+ \qquad (k = 800\ M^{-1}s^{-1}) \qquad (S1)$$

$$HOBr + HCN \rightarrow BrCN + H_2O \qquad (k = 10\ M^{-1}s^{-1}) \qquad (S2)$$

$$OBr^- + CN^- + H_2O \rightarrow BrCN + 2OH^- \qquad (k = 5.7 \times 10^7\ M^{-1}s^{-1}) \qquad (S3)$$

$$HOBr + CN^- \rightarrow BrCN + OH^- \qquad (k = 4.2 \times 10^9\ M^{-1}s^{-1}) \qquad (S4)$$

So, the formation of BrCN from HCN is highly pH dependent, slower at lower pHs. This is a result both of the slower rate constants of the parent compounds compared to the conjugate anions, and the lower solubility of HCN (pKa=9.4) at atmospheric pHs. The main liquid-phase reactions of HOBr that perpetuate the bromine explosion are the acid-assisted mechanism (Roberts et al., 2014):

$$HOBr + X^- \leftrightarrow HOBrX^- \qquad k_1, k_{-1} \qquad (S5)$$

$$HOBrX^- + H^+ \rightarrow H_2O + BrX \qquad k_H \qquad (S6)$$

$$HOBrX^- \rightarrow OH^- + BrX \qquad k_0 \qquad (S7)$$

$$k^{II} = \{k_1(k_0 + k_H[H^+])\}/\{k_{-1} + k_0 + k_H[H^+]\} \qquad (EqS1)$$

and are also pH dependent, but in the opposite sense. For Br_2/HOBr/OBr^- reacting with HCN/CN^- be a significant source of BrCN reactions S1-S4 would have to compete with reactions S5-S7 in the liquid (liquid-like or quasi-liquid layer) phase.

The rates of HOBr reaction that leads to BrCN formation can be estimated based on the above rate constants and pH dependencies, and measured ambient HCN mixing ratios (range 100 to 500 pptv). The liquid phase concentrations of HCN/CN^- as a function of pH can be estimated from the intrinsic Henry's Law solubility of HCN (H*), recognizing that for a weak acid the effective Henry's Law solubility (H_{eff}) is given by:

$$H_{eff} = H^*(1+K_a/[H^+]) \qquad (EqS2)$$

where K_a is the acid dissociation constant for HCN, and H_{eff} and H* have units of M/atm. The intrinsic solubility of HCN as a function of temperature shows the expected inverse exponential relationship with temperature (Fig. S16) and for the purposes of this work, we will assume that this relationship can be extrapolated to temperatures as low as 263K. This H*(T), Equation (1), and the acid dissociation of HCN are used to estimate [HCN] and [CN^-] assuming equilibrium with ambient HCN, and the acid dissociation of HOBr (pKa =8.6) along with the rates of S(2-4) give the estimated loss rates of HOBr (d[HOBr]/[HOBr]/dt) as a function of pH shown in Fig. S17.

The competing reactions of HOBr with $Br^-$and Cl^- as a function of pH can also be estimated from the acid dissociation of HOBr and the rates of R1&S5, assuming the surface concentrations of Cl^- and Br^- are the range measured in surface snow in the Arctic, 16μM. The results of those estimates are also shown in Fig. S17, and have the opposite relationship with pH. The two pathways are of equal importance somewhere around pH=7, however, considering the uncertainties of the above analysis, a range of pH=6-8 is probably more realistic.

2 Box Model

The basic box model used to assess possible BrCN formation is described by Wang and Pratt (2017)(Wang and Pratt, 2017). The chemistry from Reactions S1–4 and the pH dependent solubility of HCN (Equation S2) were added to the model and the conditions found during the 4/27/2018 MA were used to initialize the model. The results of the model, shown in Fig. S18, show the same pH dependence from the HOBr competitive reaction analysis. The absolute amount of BrCN is lower than observed, however it should be noted that loss rates and mechanisms of BrCN in this environment are currently unknown.

Figures

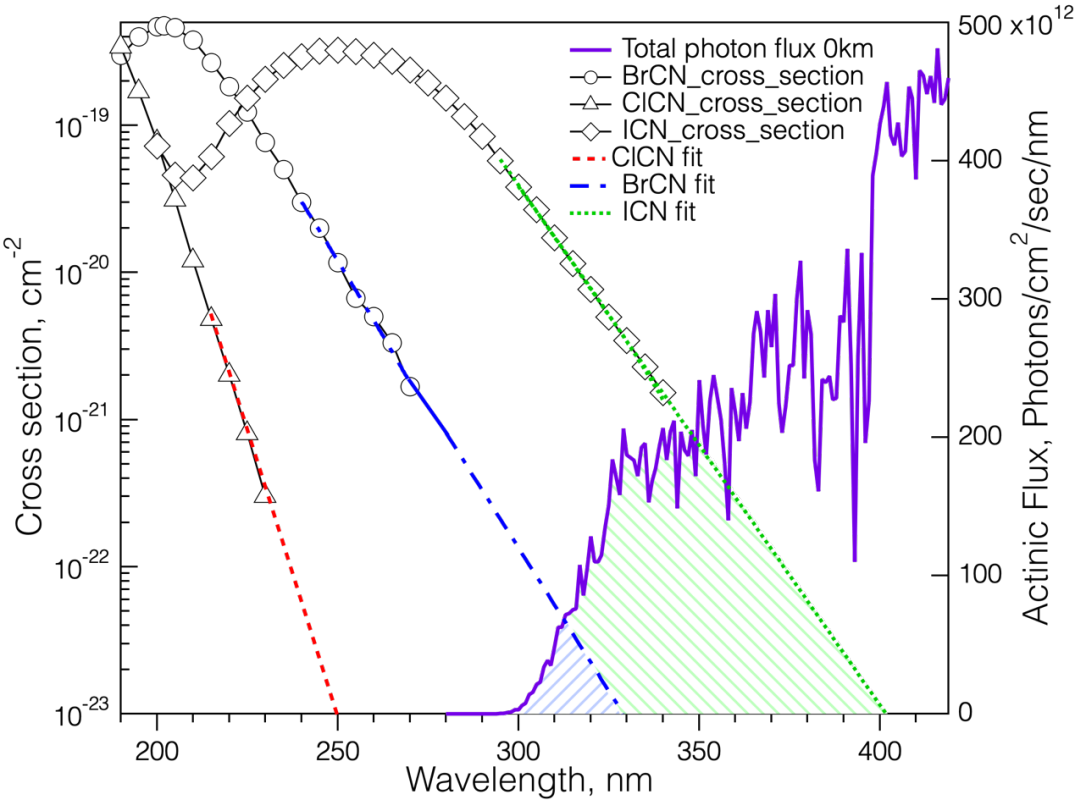

Figure S1. The UV-visible absorption spectra of ClCN, BrCN, and ICN, (Felps et al., 1991;Barts and Halpern, 1989;Russell et al., 1987;Hess and Leone, 1987), and the photon flux spectrum estimated from the NCAR TUV model for 40° N, at the surface on June 30, 2015 (NCAR, 2018). The extrapolations assume the cross-sections are log-linear over the portions that tail into the actinic region. The cross-hatched shaded areas denote the regions in which BrCN and ICN overlap with the solar flux.

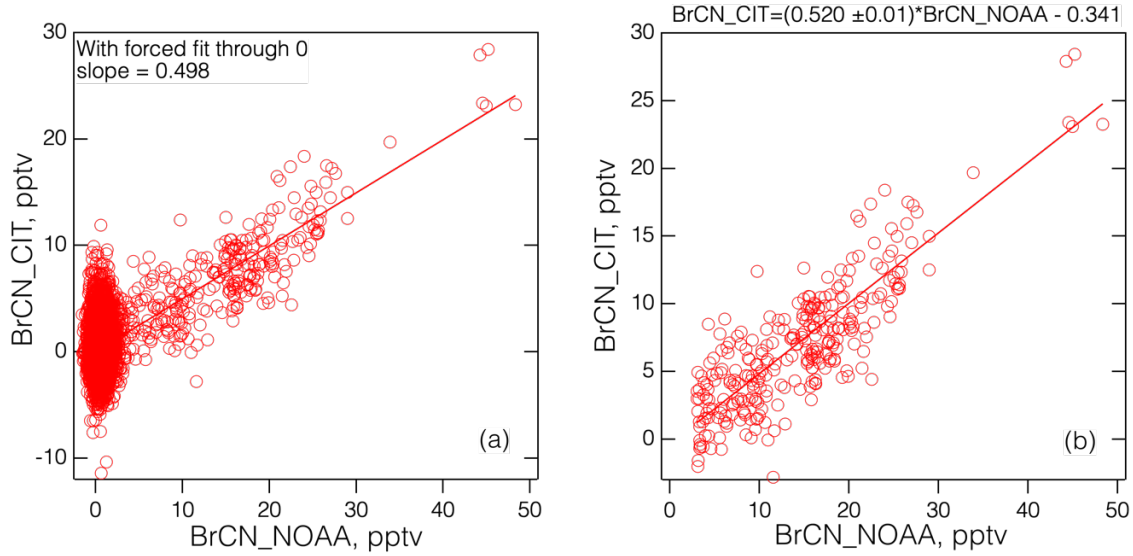

Figure S2. Plots of CIT-CIMS BrCN versus I-CIMS BrCN for both Apr. 27, 2018 and May 19, 2018 flights during ATom-4 as originally calibrated by each group. Panel (a) includes all the data and panel (b) includes only the data for which the I-CIMS BrCN was above 3 pptv. The fit line in panel (b) is from an ODR that assumes uncertainty in each variable.

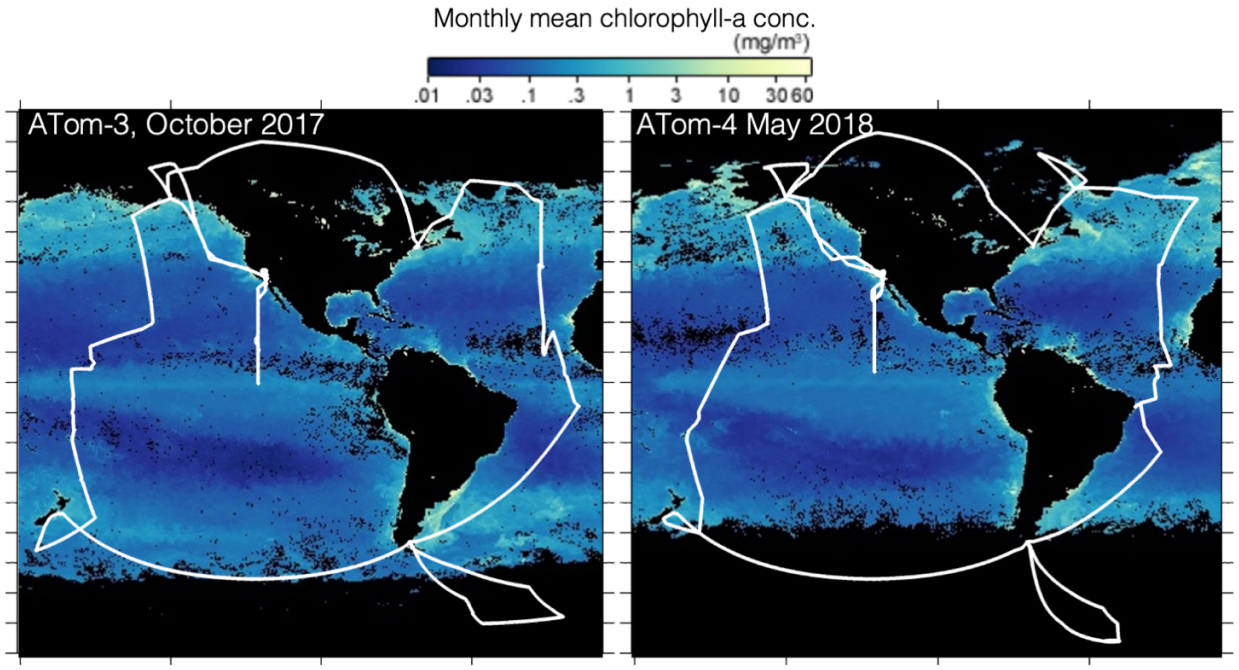

Figure S3. Maps of surface chlorophyll α concentrations estimated from satellite observations (https://neo.gsfc.nasa.gov/view.php?datasetId=MY1DMM_CHLORA) for the main months of the ATom-3 (right panel) and ATom-4 (left panel) deployments. The black regions are either areas that had too much ice cover to permit a retrieval, or are land masses.

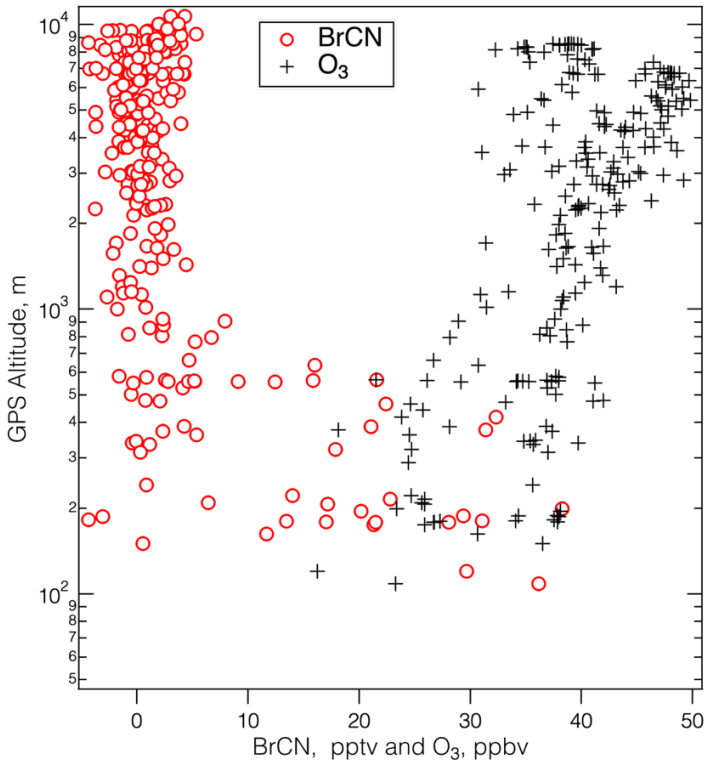

Figure S4. The ATom-2 BrCN and O_3 measurements as a function of altitude for both Arctic flights. The measurements were averaged over the UCI-WAS sample time to be compatible with the data in Fig. 4 in the main text. The BrCN values are shown as red circles and the O_3 values are shown as black crosses.

Figure S5. An image from the nose camera video of the DC-8 taken at 23:40:11 UTC during the low-level leg of the Oct. 11, 2017 flight described in the main text. The videos acquired on the aircraft were stored as .mkv files (https://asp-archive.arc.nasa.gov/), converted to .avi files via MATLAB and stored on Google Drive. The videos were then played directly by Document Viewer for Google Drive.

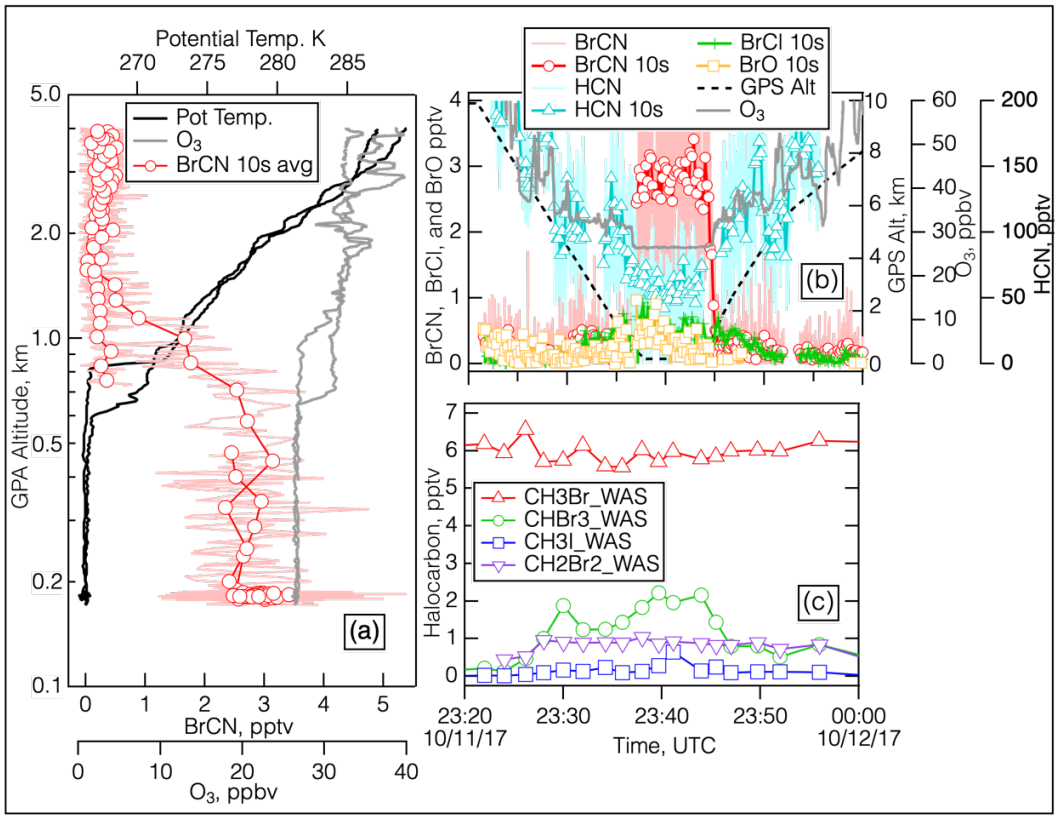

Figure S6. Details of the measurements during the polar boundary layer leg of the Oct. 11, 2017 flight over the Southern Ocean centered around 23:40 UTC. The left panel are the altitude profiles of potential temperature, O_3 and BrCN (10 s avg). The top right panel shows the time series for BrCN, BrCl, BrO, HCN, O_3, and altitude. The bottom right panel shows the time series for the halocarbons, CH_3Br, CH_3I, CH_2Br_2 and $CHBr_3$.

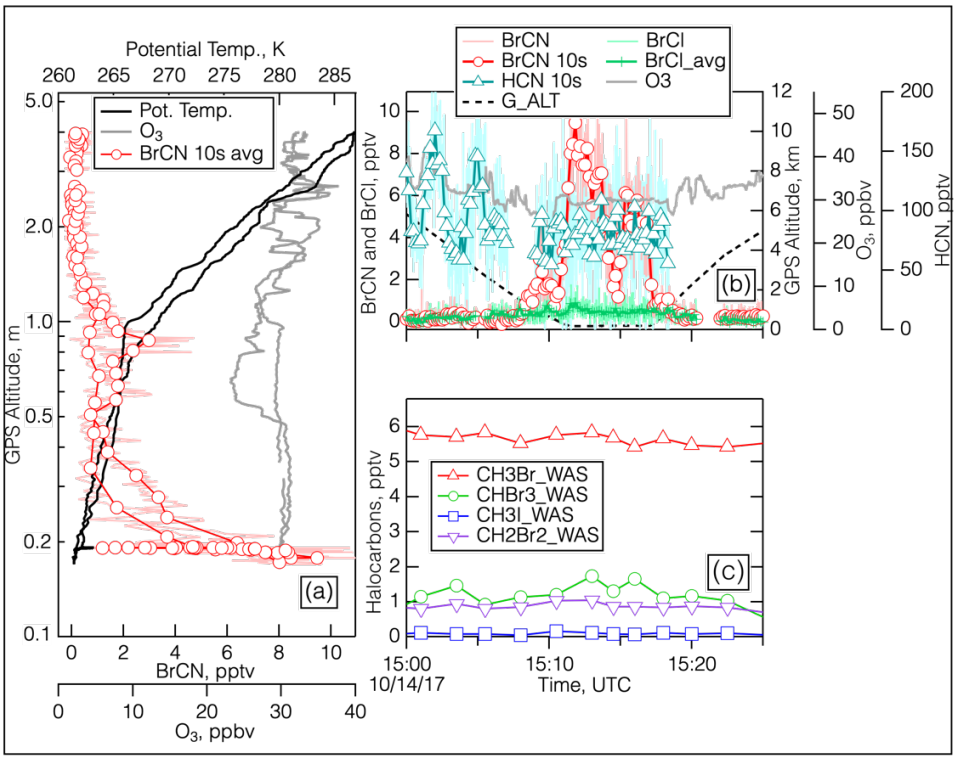

Figure S7. Details of the measurements during the polar boundary layer leg of the Oct. 14, 2017 flight centered around 15:15 UTC. Panel (a) shows the altitude profiles of potential temperature, O_3 and BrCN (10 s avg). Panel (b) shows the time series of BrCN, BrCl, HCN, O_3, and altitude. Panel (c) shows the time series of the halocarbons, CH_3Br, CH_3I, CH_2Br_2 and $CHBr_3$.

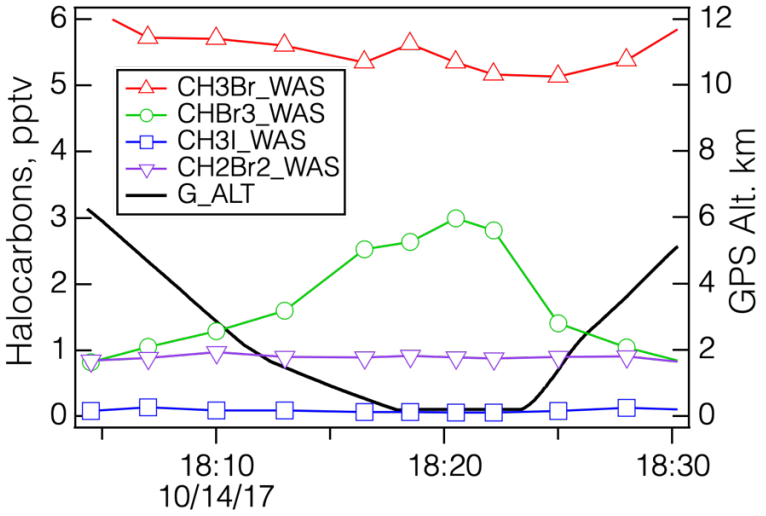

115 **Figure S8. The time series of halocarbons, CH_3Br, CH_3I, CH_2Br_2, $CHBr_3$, and GPS altitude measured around the polar boundary layer leg centered around 18:20 during the Oct. 14, 2017 flight.**

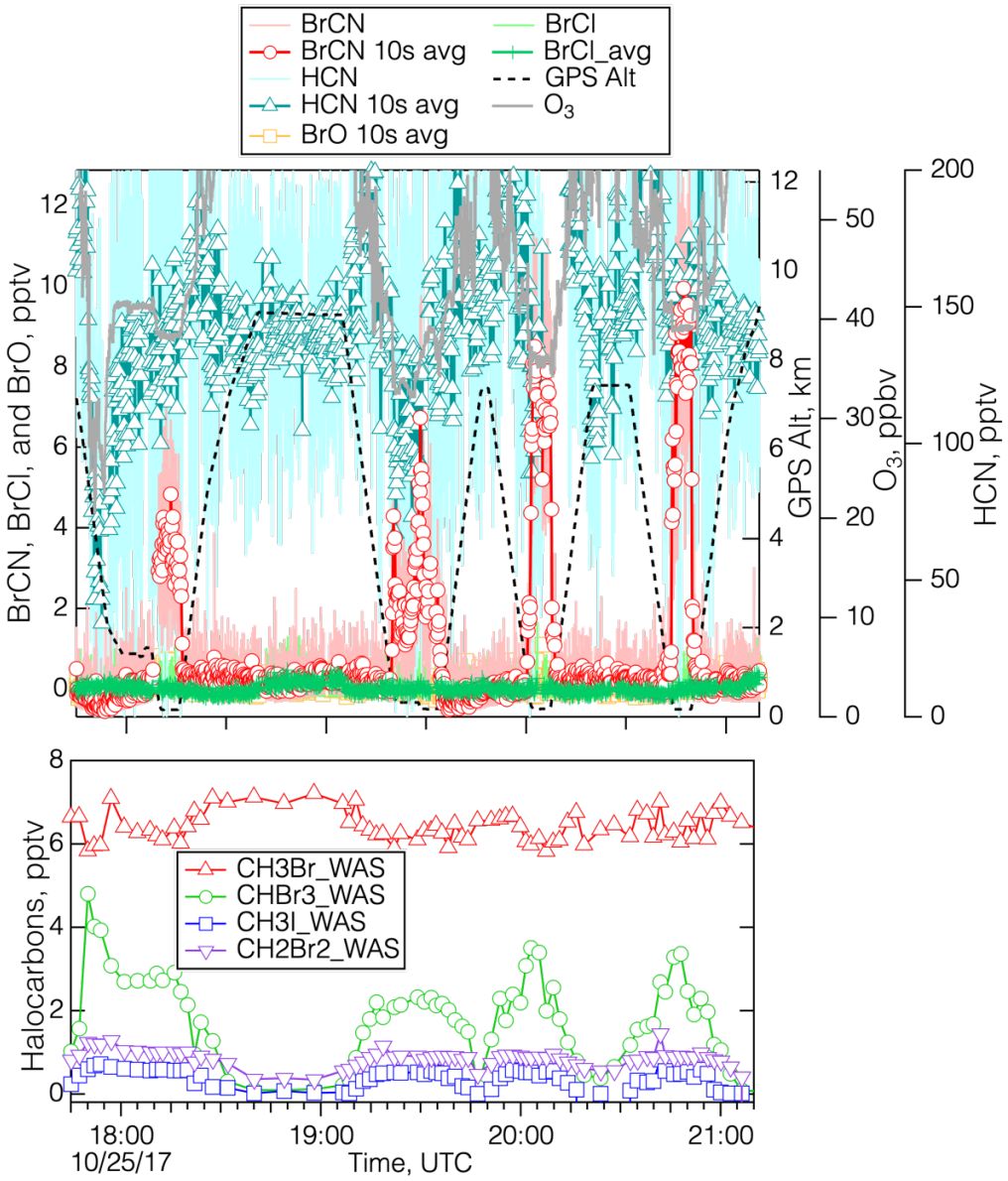

Figure S9. Details of the measurements during the polar boundary layer legs of the Oct. 25, 2017 flight when BrCN above detection limit was observed. The top panel shows the time series for BrCN, BrCl, BrO, HCN, O_3, and altitude, and the bottom panel shows the time series for the halocarbons CH_3Br, CH_3I, CH_2Br_2, and $CHBr_3$.

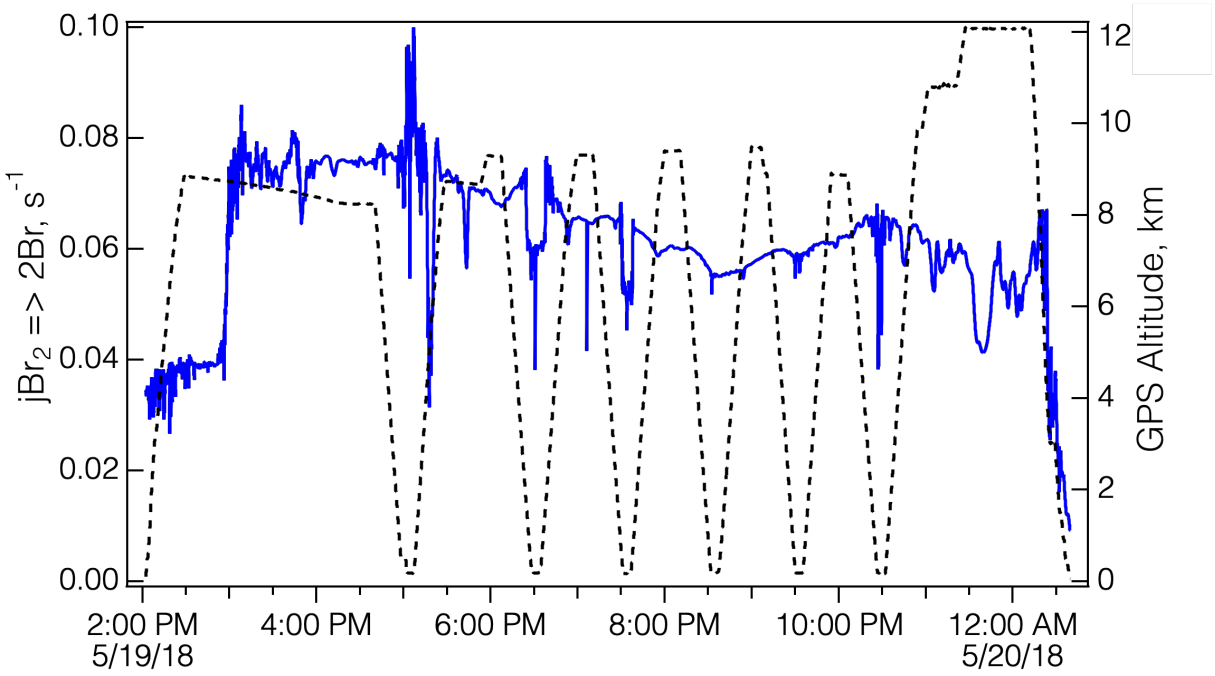

Figure S10. The time series of $jBr_2 \rightarrow 2$ Br (solid blue line) for the ATom-4 flight on May 19, 2018, plotted along with altitude (dashed black line).

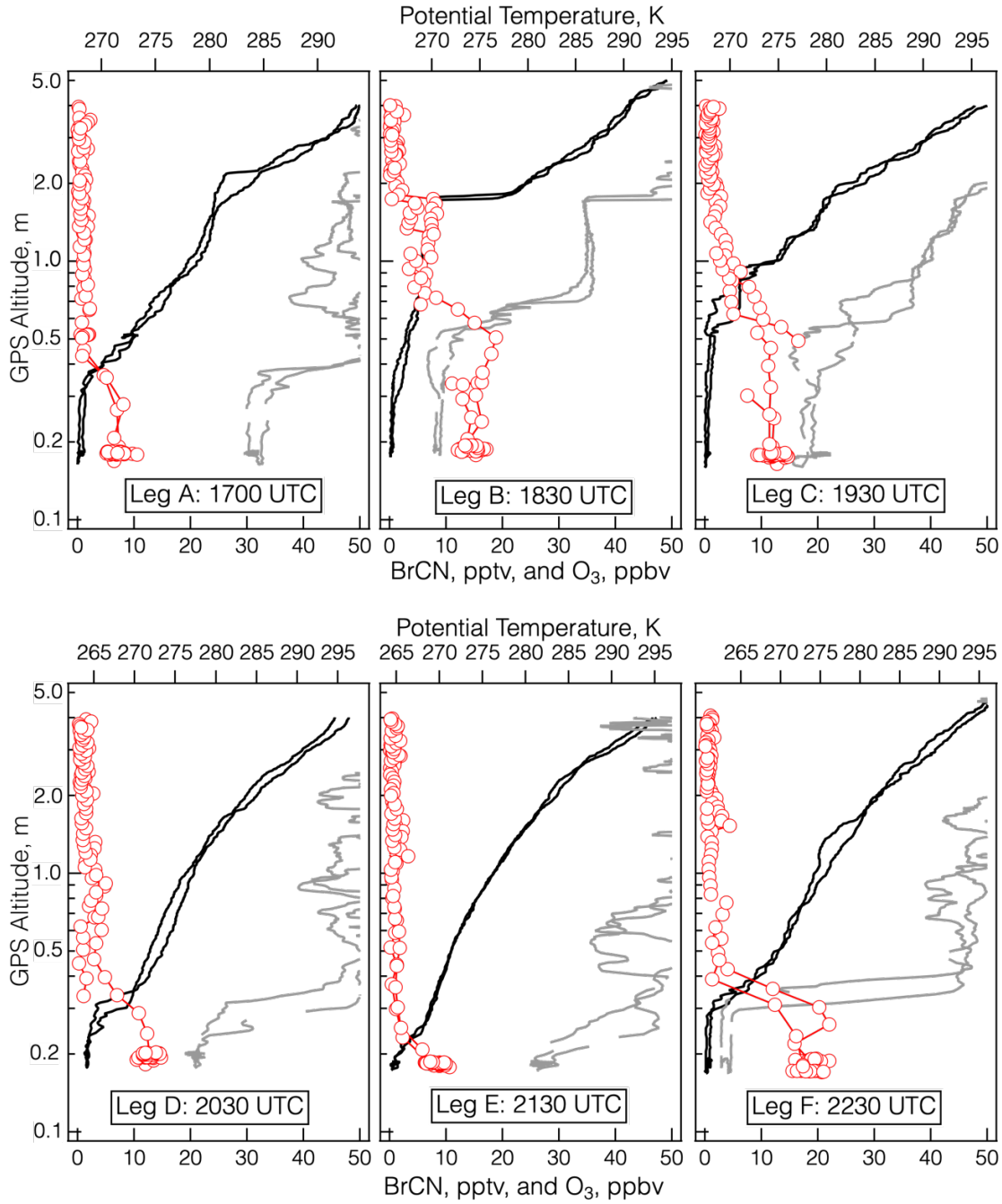

Figure S11. The vertical profiles for potential temperature (black), O_3 (grey) and BrCN 10 s averages (red circles) for the 6 polar boundary layer legs during the Oct. 19, 2018 flight shown in detail in Fig. 6 and 7.

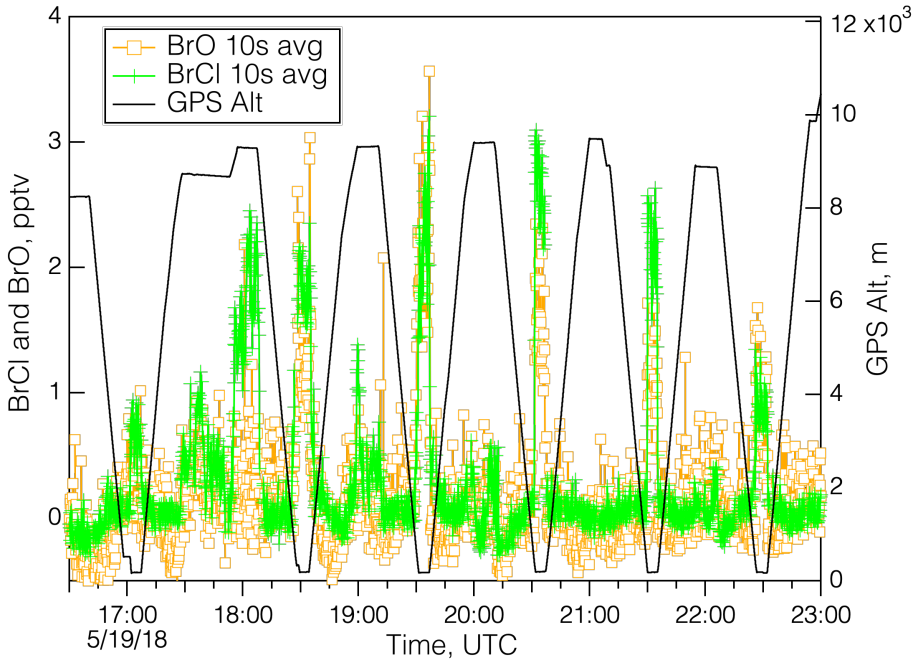

Figure S12. Measurements of BrO and BrCl during the Oct. 19, 2018 flight from Bangor, ME, to Anchorage, AK. The altitude is shown in black, BrO is shown as orange squares, and BrCl is shown as green crosses.

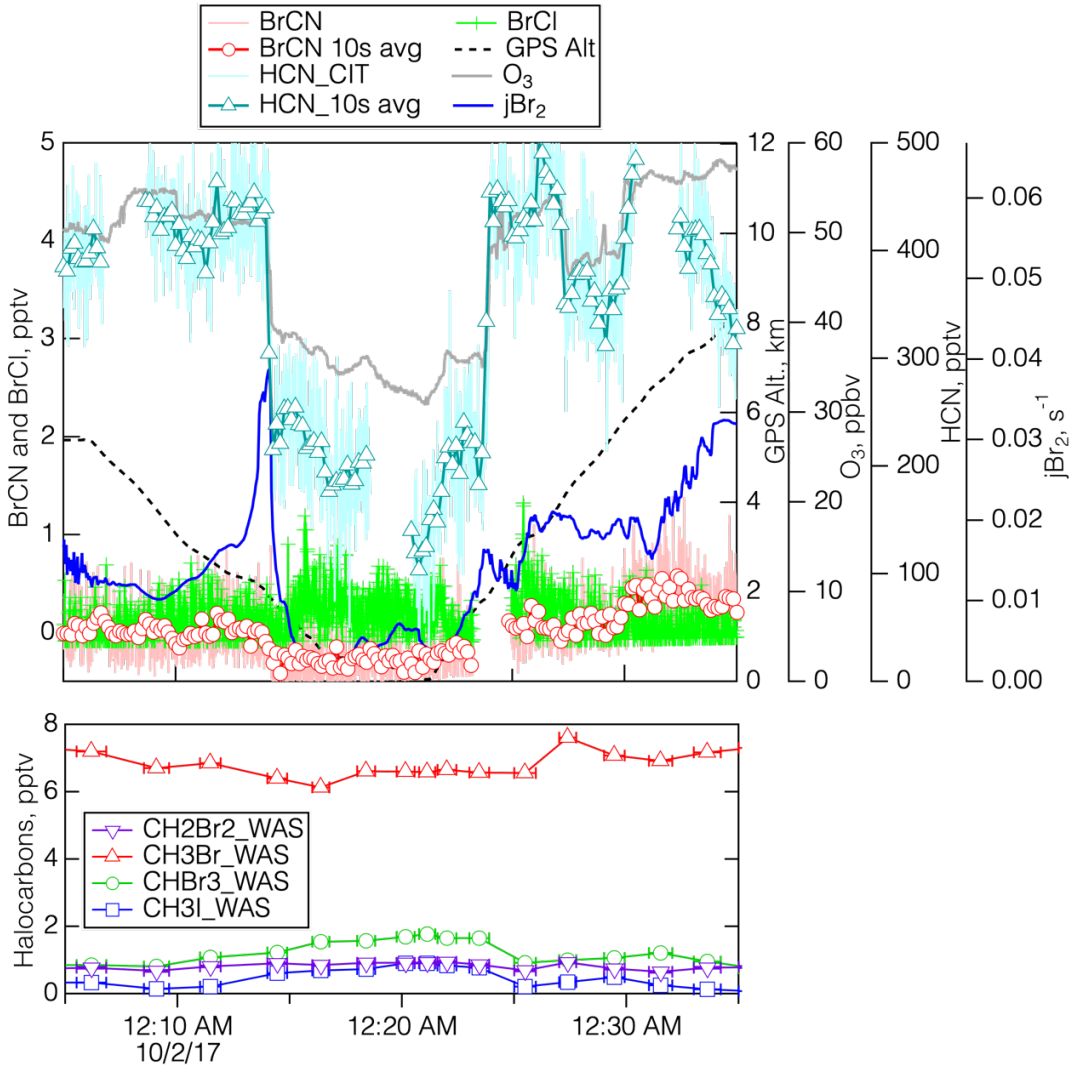

130

Figure S13. Details of the measurements during the polar boundary layer legs of the Oct. 01, 2017 flight during the MA over BRW. The top panel shows the time series for BrCN, BrCl, HCN, O_3, jBr_2, and altitude, and the bottom panel shows the time series for the halocarbons CH_3Br, CH_3I, CH_2Br_2, and $CHBr_3$ measured by the whole-air sampler.

Figure S14. An image from the nose camera video of the DC-8 taken at 00:20:29 (Oct. 02, 2017) UTC during the MA over BRW as part of the Oct. 01, 2017 flight described in the main text. Note the presence of low-level clouds. The videos acquired on the aircraft were stored as .mkv files (https://asp-archive.arc.nasa.gov/), converted to .avi files via MATLAB and stored on Google Drive. The videos were then played directly by Document Viewer for Google Drive.

Figure S15. The top panel shows a Google Earth view of BRW and the city of Utqiagvik, AK. The wind vector that corresponded to the wind direction during the lowest 2.5 km of the Apr. 27, 2018 MA is shown as the red arrow. The end of the BRW runway is very close to the shore of the Arctic Ocean, which had packed ice during the 4/27/18 MA as shown in the bottom panel taken at Apr. 28, 2018 00:35:39 from the video camera in the nose of the DC-8. The videos acquired on the aircraft were stored as .mkv files (https://asp-archive.arc.nasa.gov/), converted to .avi files via MATLAB and stored on Google Drive. The videos were then played directly by Document Viewer for Google Drive.

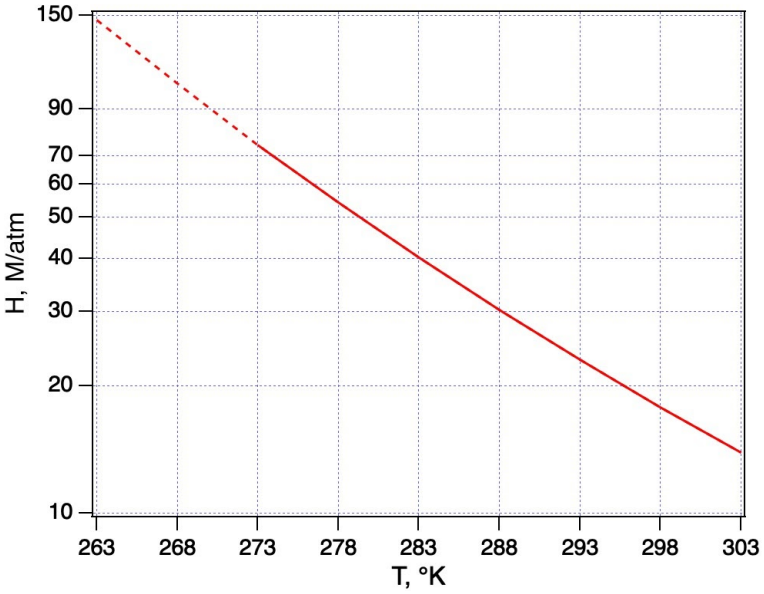

Figure S16. The Henry's Law solubility of HCN versus temperature (Yoo et al., 1986) extrapolated below the freezing point assuming that the same thermodynamic parameters apply.

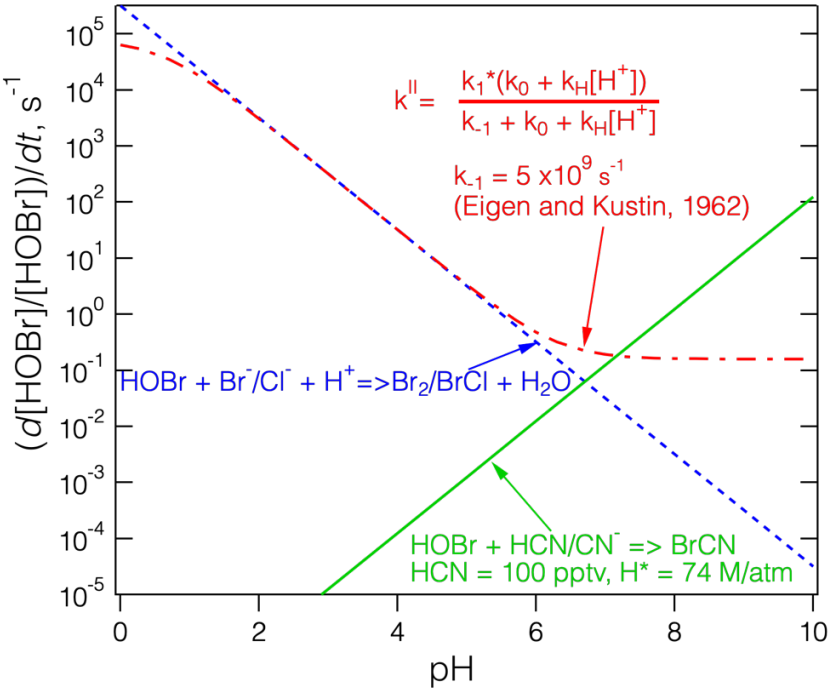

Figure S17. The relative loss rate of HOBr for either reaction with halides using either the traditional acid dependent model (blue dashed line), the acid assisted model (red dot-dashed line), or reaction with HCN/CN^- (green solid line) as a function of pH under the conditions specified.

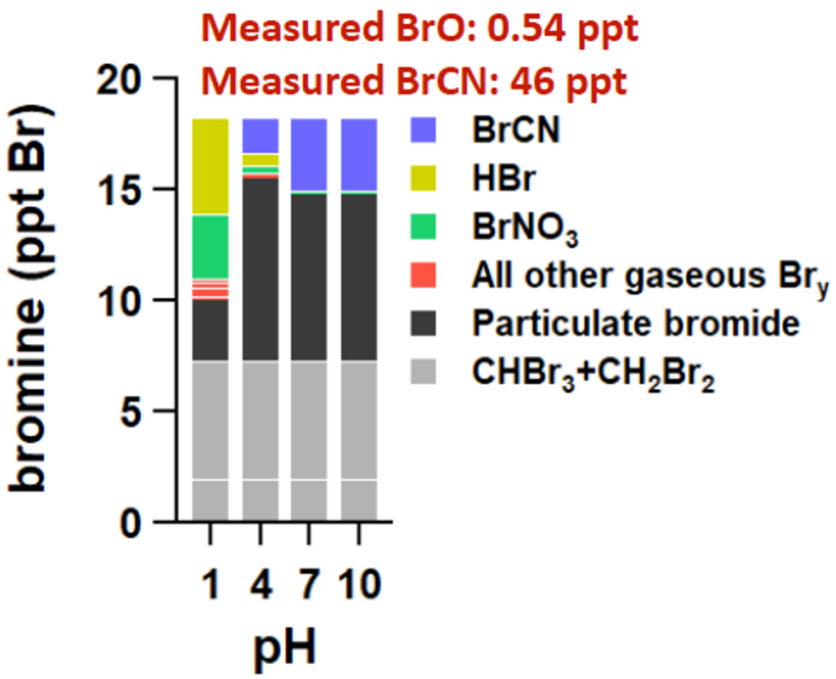

160 **Figure S18. The result of the box model for Apr. 27, 2018 as a function of pH.**

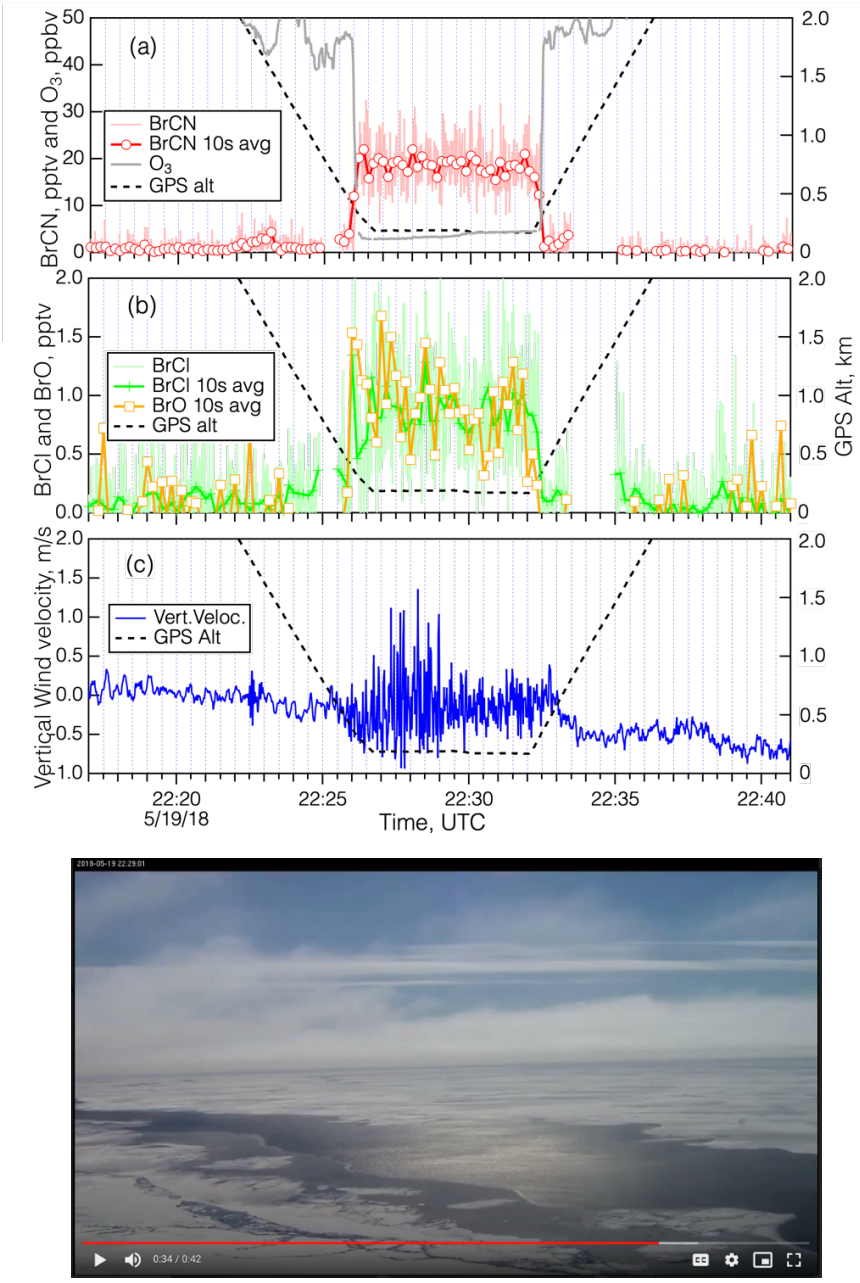

Figure S19. Details of the polar boundary layer leg on May 19, 2018, centered at 22:30. Panel (a) shows BrCN, O_3 and GPS altitude. Panel (b) shows BrCl (1 s and 10 s avg) and BrO (10 s avg). Panel (c) shows the vertical wind velocity measured aboard the DC-8 aircraft during the polar boundary layer leg. The bottom panel is an image from the DC-8 nose video camera taken at 22:29 UTC. The videos acquired on the aircraft were stored as .mkv files (https://asp-archive.arc.nasa.gov/), converted to .avi files via MATLAB and stored on Google Drive. The videos were then played directly by Document Viewer for Google Drive.

Table S1. Properties of Cyanogen Halides, FCN, ClCN, BrCN, ICN, and HCN, $(CN)_2$ and HCN (Davis and Okabe, 1968)

Compound	Exact Mass	MP, °C	BP, °C	P_{vap}, Torr	D(X-CN), Kcal/mole†
FCN	45.0015	–	-46	Gas	111 ±0.8
ClCN	60.9719*	-6.55	13	Gas	97 ±1
BrCN	104.9214*	50–53	61–62	21 @0°C 119 @25 °C	83 ±1
ICN	152.9076	146.7	–	0.9 @25 °C	73 ±1
$(CN)_2$	52.0061	-28	-21.1	Gas	128 ±1
HCN	27.0109	-13.3	26	750 @25 °C	120 ±1

† D(C≡N) = 184 ±1

* Exact mass of the lowest isotopologue, ie., ^{35}ClCN and ^{79}BrCN.

Table S2. Halogen species measured by the I-ToF-CIMS and associated parameters. The BrCN values resulted from the comparison of the CIT-CIMS and I-CIMS data sets as described in the Methods section.

Compound	Precision, pptv	Accuracy	Detection Limit, pptv
BrO	0.3	25% + 0.2 pptv	0.6
BrCl	0.2	25% + 0.4 pptv	1.2
Cl_2	0.2	15% + 0.4 pptv	1.2
$ClNO_2$	0.1	15% + 0.05 pptv	0.15
BrCN	1	25% + 0.3 pptv	1.1

References

Barts, S. A., and Halpern, J. B.: Photodissociation of ClCN between 190 and 213 nm, J. Phys. Chem., 93, 7346-7351, 1989.
Davis, D. D., and Okabe, H.: Determination of bond dissociation energies in hydrogen cyanide. Cyanogen and cyanogen halides by the photodissociation method, J. Chem. Phys., 49, 5526-5531, 10.1063/1.1670082, 1968.
Felps, W. S., Rupnik, K., and McGlynn, S. P.: Electronic spectroscopy of the cyanogen halides J. Phys. Chem., 95, 639-656, 1991.
Hess, W. P., and Leone, S. R.: Absolute I* quantum yields for the ICN Ã state by diode laser gain-vs-absorption spectroscopy, J. Chem. Phys., 86, 3773-3780, 1987.
Li, Q., Jacob, D. J., Yantosca, R. M., Heald, C. L., Singh, H. B., Koike, M., Zhao, Y., Sachse, G. W., and Streets, D. G.: A global three-dimensional model analysis of the atmospheric budgets of HCN and CH_3CN: Constraints from aircraft and ground measurements, J. Geophys. Res. Atmos., 108, 10.1029/2002JD003075, 2003.
Quick TUV Calculator: http://cprm.acom.ucar.edu/Models/TUV/Interactive_TUV/, access: September 1, 2018, 2018.
Roberts, T. J., Jourdain, L., Griffiths, P. T., and Pirre, M.: Re-evaluating the reactive uptake of HOBr in the troposphere with implications for the marine boundary layer and volcanic plumes, Atmos. Chem. Phys., 14, 11185-11199, 10.5194/acp-14-11185-2014, 2014.
Russell, J. A., McLaren, I. A., Jackson, W. M., and Halpern, J. B.: Photolysis of BrCN between 193 and 266 nm, J. Phys. Chem., 91, 3248-3253, 1987.
Wang, S., and Pratt, K. A.: Molecular halogens above the Arctic snowpack: Emissions, diurnal variations, and recycling mechanisms, J. Geophys. Res. Atmos., 122, 11,991-912,007, 10.1002/2017JD027175, 2017.
Yoo, K.-P., Lee, S. Y., and Lee, W. H.: Ionization and Henry's Law constants for volatile, weak electrolyte water pollutants, Korean J. Chem. Eng., 3, 67-72, 10.1007/BF02697525, 1986.